


Nonseparable Polarization Wavefront Transformation

 Zhujun Shi,¹ Noah A. Rubin,¹ Joon-Suh Park,^{1,2} and Federico Capasso¹
¹*John A. Paulson School of Engineering and Applied Sciences, Harvard University, Cambridge, 02138 Massachusetts, USA*
²*Nanophotonics Research Center, Korea Institute of Science and Technology (KIST), Seoul 06600, South Korea*
 (Received 2 January 2021; accepted 5 April 2022; published 12 October 2022)

In this Letter, we investigate a new class of polarization wave front transformations which exhibit nonconventional far field interference behavior. We show that these can be realized by double-layer metasurfaces, which overcome the intrinsic limitations of single-layer metasurfaces. Holograms that encode four or more distinct patterns in nonorthogonal polarization states are theoretically demonstrated. This Letter clarifies and expands the possibilities enabled by a broad range of technologies which can spatially modulate light's polarization state and, for metasurfaces specifically, rigorously establishes when double-layer metasurfaces are—and are not—required.

DOI: 10.1103/PhysRevLett.129.167403

Traditionally, wave front transformation is characterized by a scalar function—a spatially varying phase and amplitude profile. Recently, its scope has been extended to incorporate the polarization degree of freedom—the polarization state of light can be adjusted spatially [1–6]. In a typical application, these devices are designed to implement two independent phase profiles for a pair of orthogonal polarization states. In this way, a single device can function as two different ones, controlled by the incident polarization [Fig. 1(a) shows this schematically for a metasurfacelike device].

What happens if the incident polarization state differs from the designed ones? For most previous devices, one simply gets a weighted intensity sum of the two designed patterns in the far field [Fig. 1(d)]. However, we point out here that this intuitive intensity addition rule does not hold in general. In this Letter, we show that there exists a class of intriguing polarization wave front transformations [Fig. 1(e)], where the output intensity pattern may change dramatically for different input polarization states. In this case, the far field electric field for two orthogonal incident polarization states may interfere with each other, leading to nonintuitive polarization-dependent behavior [Figs. 1(f)–1(h)]. For example, one can project a triangle and rectangle for x and y incident polarization [Figs. 1(f)–1(g)], and obtain a circle for 45 degree incident polarization [Fig. 1(h)]. This is in sharp contrast to previous polarization holograms, which can encode only two images.

As we will show later, a distinguishing feature of such wave front transformations [Fig. 1(e)] is that the output field's spatial and polarization degrees of freedom are *always* nonseparable for *any* plane wave incidence. In contrast, for most previous devices, one can find a pair of orthogonal incident states, where the output polarization is uniform across the wave front, and thus separable [7]. We refer to them as nonseparable and separable polarization wave front

transformations respectively. [See Appendix, Sec. 1.1 Refs. [8–17] for further discussions on (non)separable states of light versus (non)separable transformations.]

To understand their far field polarization behavior, let us revisit the concept of orthogonality. Consider two plane waves incident normal to a polarization element with orthogonal polarization states. Neglecting losses and nonlinearity, orthogonality requires that the inner product of the two output far fields, $\vec{E}_1(x, y)$ and $\vec{E}_2(x, y)$, to be zero,

$$\int \vec{E}_1^*(x, y) \cdot \vec{E}_2(x, y) dx dy = 0. \quad (1)$$

Equation (1) holds for both separable and nonseparable transformations. However, the implications are very different.

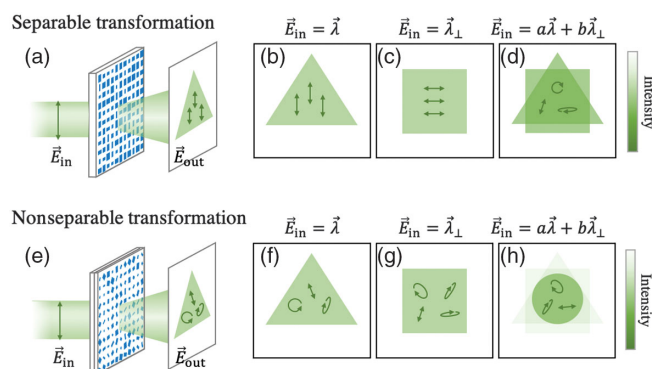


FIG. 1. (a),(b) Schematics of separable and nonseparable transformations. (c)–(h) The output far field patterns for different incident polarization states. $\vec{\lambda}$ and $\vec{\lambda}_\perp$ are orthogonal. Among them, (b) and (c) are separable states; (d) and (f)–(h) are nonseparable states. In terms of far field superposition, (d) is an intensity sum of (b) and (c), whereas (h) shows a new pattern that is different from (f) or (g).

TABLE I. Properties of separable and nonseparable transformations. $t_{ij}(x, y)$ are spatial functions. V and U are the basis transformation matrices for the input and output electric field respectively, and are constant across the wave front. Note that V and U can be different.

	Jones matrix (J)	Polarization channels	Far field superposition
Separable transformation	$U \begin{pmatrix} t_{11}(x,y) & 0 \\ 0 & t_{22}(x,y) \end{pmatrix} V^\dagger$	2	Intensity sum
Non-separable transformation	$U \begin{pmatrix} t_{11}(x,y) & t_{12}(x,y) \\ t_{21}(x,y) & t_{22}(x,y) \end{pmatrix} V^\dagger$	4	Interference pattern

For the former, we can write $\vec{E}_{1(2)}(x, y) = f_{1(2)}(x, y)\hat{u}_{1(2)}$, where $f_{1(2)}(x, y)$ are the complex amplitudes, and $\hat{u}_{1(2)}$ are polarization vectors. As $\hat{u}_{1(2)}$ are independent of spatial coordinates, Equation (1) becomes

$$(\hat{u}_1^* \cdot \hat{u}_2) \int f_1^*(x, y)f_2(x, y)dxdy = 0. \quad (2)$$

The complex amplitudes f_1 and f_2 can be arbitrary spatial functions chosen by design. Therefore in general $\int f_1^*f_2dxdy \neq 0$, which implies that $\hat{u}_1^* \cdot \hat{u}_2 = 0$, and thus $\vec{E}_1^*(x, y) \cdot \vec{E}_2(x, y) = 0$. In other words, the local electric fields are orthogonal to each other everywhere. As a result, there is no interference between them. The far field intensity pattern for any other incident polarization state will simply be a weighted sum of $|\vec{E}_1(x, y)|^2$ and $|\vec{E}_2(x, y)|^2$.

However, the situation changes completely for nonseparable polarization wave front transformations. In this case, the far field polarization states $\hat{u}_{1(2)}(x, y)$ vary spatially, and cannot be considered independently from the integral as in Eq. (2). The local orthogonality does not hold any more. In fact, $\vec{E}_1^*(x, y) \cdot \vec{E}_2(x, y)$ can be nonzero almost everywhere, as long as their spatial integral cancels out. Therefore, at any location on the wave front, $\vec{E}_1(x, y)$ and $\vec{E}_2(x, y)$ can have a nonvanishing interference term, which opens up an entire new design space for polarization control.

The above discussion can be made more rigorous by considering the near-to-far field transformation of light (Appendix, Sec. 1.2). Immediately after light passes through a lossless polarization element, the local orthogonality is preserved. However, during propagation, secondary waves emitted from different locations on the device start to overlap spatially, which leads to nonorthogonality in the far field.

Mathematically, a polarization wave front transformation is described by a spatially varying two-by-two Jones matrix profile $J(x, y)$, where each matrix element is a spatial function [17,18] (Table I). For separable transformations, the Jones matrices at *different* locations across the wave front can be diagonalized *simultaneously*.

However, for nonseparable transformations, there are always nonvanishing off diagonal elements for any *global* polarization basis. This also results in their different information capacity. Separable transformations have only two usable polarization channels t_{11} , t_{22} , whereas for nonseparable transformations, t_{11} , t_{12} , t_{21} , t_{22} can all be designed to have different spatial profiles. Therefore, the latter can encode more optical functions in a single device, and may find applications in optical communication and quantum optics.

The Jones matrix formalism can be used for both near field and far field, which are related by Fourier transforms [17]. The properties listed in Table I hold for both. From a device design perspective, it is usually more convenient to work with near-field Jones matrices, which characterize the change of polarization states immediately before and after the device. In the following, we assume near-field Jones matrix profiles by default, with the prefix omitted. For lossless polarization elements, the (near field) Jones matrix profiles are unitary, and can be visualized using the geometrical representation introduced in the next section.

Geometrical representation.—To facilitate the analysis, we introduce a new geometrical representation of Jones matrices. It allows us to intuitively visualize any Jones matrix profile, just as we can plot out the phase profile of a phase-only element.

For any unitary Jones matrix, we define a corresponding retarder parameter:

$$\mathbf{R} = \sin \frac{\alpha}{2} \hat{n}, \quad \alpha \in (-\pi, \pi] \quad (3)$$

where $\hat{n} = (n_1, n_2, n_3)$ is the Stokes vector of the eigenpolarization state of the Jones matrix, and α is the phase retardation [7,9]. The overall phase is omitted, so for any choice of α Eq. (3) actually represents a class of Jones matrices, all having the same polarization effect, but may have different overall phases. Some equivalent expressions of \mathbf{R} are given in Table S1 in the Supplemental Material [19].

Using this definition, we can intuitively visualize any unitary Jones matrix. Taking the three components (R_1, R_2, R_3) as the Cartesian coordinates, it can now be represented as a point in the 3D space [Fig. 2(a)]. Polarization wave front transformations, which are described by spatial functions of Jones matrices, can now be represented as curves or surfaces, or collections of points, if sampled discretely, in the retarder space [Figs. 2(b)–2(f)].

Using this representation, we can intuitively distinguish separable and nonseparable transformations simply by observing their geometrical shapes in the retarder space. In fact, we prove that in general a separable transformation is represented by an ellipse [(Fig. 2(b); Appendix, Sec. 5.4). Nonseparable transformations, on the other hand, may have arbitrary shapes or trajectories [Fig. 2(c)].

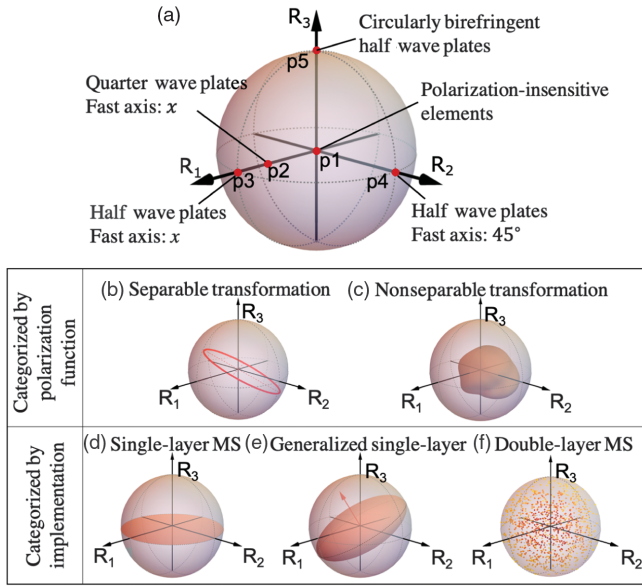


FIG. 2. (a) Schematics of the retarder space. Each point represents a class of unitary Jones matrices (wave plates) with the same polarization effect, up to some overall phase. The radial distance and orientation are related to the phase retardation and the eigenpolarization states respectively. For example, points 1–3 have the same fast axis along x , but varying retardance, from zero to quarter wave to half wave. Points 3–5 are all half wave plates, but with different eigenpolarizations states. In particular, points in the equatorial plane correspond to linearly birefringent elements. (b)–(f) A polarization wave front transformation can be represented in the retarder space as a curve or surface or a collection of points. (b) Separable transformations are mapped to ellipses. (c) Nonseparable transformations can have arbitrary shapes. (d)–(f) Polarization transformations by single-layer, generalized single-layer, and double-layer metasurfaces are represented by the equatorial plane, ellipsoids, and arbitrary shapes or points respectively.

Implementation with metasurfaces.—Recently, metasurfaces—artificial interfaces patterned with subwavelength arrays of nanostructures [5,20,21]—have emerged as an exciting new medium in polarization optics. Each nanostructure functions as a linearly birefringent wave plate, whose optical axis and phase retardation can be adjusted spatially by design [7,9,22–25]. Here we use metasurfaces as a general platform for polarization wave front transformation. In particular, we propose to use double-layer metasurfaces [Fig. 3(c)] to realize nonseparable transformations.

Separable transformations can be easily realized using single-layer metasurfaces [Fig. 3(a)], combined with additional wave plates if necessary [Fig. 3(b)]. Essentially, we can design the metasurface to implement two different phase profiles for horizontal and vertical polarization, which corresponds to the Jones matrix profile $J = \begin{pmatrix} t_{11}(x,y) & 0 \\ 0 & t_{22}(x,y) \end{pmatrix}$. If needed, we can add additional wave plates to provide the global basis change U and V [Fig. 3(b)]. We refer to such implementation as generalized single-layer metasurfaces.

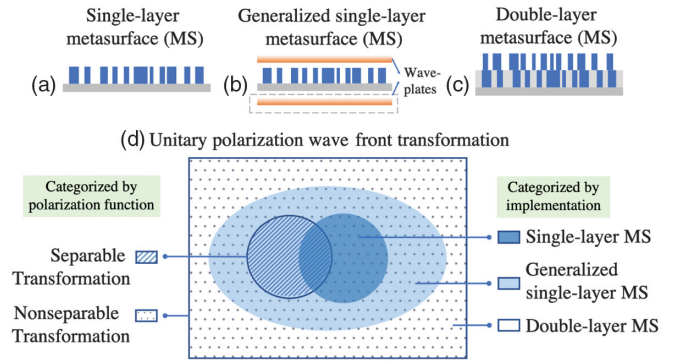


FIG. 3. (a)–(c) Side views of single-layer, generalized single-layer, and double-layer metasurfaces. (d) The Venn diagram summarizes the relation between different types of polarization transformations (marked by fill pattern) and the possible metasurface implementations (marked by color). Generalized single-layer metasurfaces (light blue) can realize all separable transformations (line pattern) and a subset of nonseparable transformations (dot pattern). Double-layer metasurfaces (dark blue) can implement any unitary polarization transformation.

According to Table I, all separable transformations can be realized in this way.

For nonseparable transformations, however, single-layer metasurfaces are not enough. In general, the required Jones matrices for nonseparable transformations can be arbitrarily birefringent—linear, circular or elliptical—across the wave front. Single-layer nanostructures, however, are constrained to be linearly birefringent due to reciprocity. (See Appendix, Sec. 4. for further discussion.) To overcome this limitation, we propose to use double-layer metasurfaces [Fig. 3(c)]. The polarization effect is accumulated upon interaction with light, i.e., $J_{\text{bilayer}} = J_{\text{top}} J_{\text{bottom}}$ (Appendix, Sec. 7.2). Although individually J_{top} and J_{bottom} are linearly birefringent, their product J_{bilayer} can be arbitrarily birefringent (Appendix, Sec. 6). Therefore, double-layer metasurfaces can achieve any unitary polarization wave front transformation, including both separable and nonseparable ones. It is noted that double-layer metasurfaces have been previously used for (polarization-independent) dispersion engineering [26], but their unique polarization transformation capabilities have not been investigated.

While it might not be surprising that two layers can realize more polarization functions than a single layer, importantly, we show that two layers are sufficient (Appendix, Sec. 6). More layers may help with the dispersion or angular response, but will not add more polarization function at the design wavelength.

Polarization wave front transformations that are achievable with different types of metasurfaces can be illustrated in the retarder space [Figs. 2(d)–2(f), Fig. S8 in the Supplemental Material [19]]. As single-layer metasurfaces are made up of linearly birefringent nanostructures, they correspond to the equatorial plane [Fig. 2(d)]. Generalized

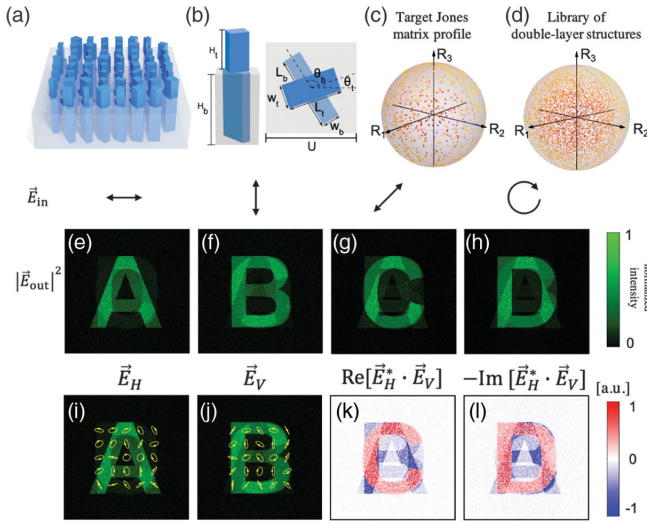


FIG. 4. (a) A schematic of the device. It consists of two layers of TiO_2 rectangular nanopillars fabricated on top of one another. The bottom layer is encapsulated in glass. The top layer is exposed to air. (b) The building blocks of the metasurface. $H_t = 600$ nm, $H_b = 1600$ nm. $U = 225$ nm. The design wavelength is $\lambda = 488$ nm. (c) The optimized target Jones matrix profile. For visualization purposes, only 1% of the points are shown. (d) The retarder space representation of the simulated library. (e)–(h) The simulated far field intensity pattern for horizontal, vertical, 45 degree, and left circular incident polarization state respectively. (i)–(j) The simulated far field polarization distribution for horizontal and vertical incident polarization. (k)–(l) The real and imaginary parts of $\vec{E}_H^* \cdot \vec{E}_V$. Red and blue correspond to positive and negative value respectively.

single-layer metasurfaces deform the plane into origin-centered ellipsoids [Fig. 2(e)] by changing the input and output polarization basis (Appendix, Sec. 5). Representing the most general case, double-layer metasurfaces can have arbitrary shapes or points in the retarder space [Fig. 2(f)].

Comparing Figs. 2(b) and 2(c) with Figs. 2(d)–2(f) reveals the relation between the polarization function and the required implementation. For example, since an ellipse is part of an ellipsoid, separable transformations can always be realized using generalized single-layer metasurfaces. For nonseparable transformations, while usually double layers are required, there are special cases where (generalized) single layers should suffice—if the required Jones matrix profile happens to belong to an ellipsoid. A summary is given in Fig. 3(d). From a practical design point of view, for a given task, one can simply plot the target Jones matrix profiles in the retarder space and determine straightforwardly whether the transformation is separable and what kind of metasurface is required for the implementation.

Multichannel polarization hologram.—In this section, we provide a concrete example of nonseparable transformations. A schematic is shown in Fig. 4(a). It is a multichannel polarization hologram that projects different far field holographic images for different incident polarization states.

For horizontal and vertical incident polarization, the device generates an image of the letter *A* and *B* respectively in the far field. The naive intensity addition rule would predict a mixture of *A* and *B* for any other incident polarization state. However, by using nonseparable transformations, we can design the device such that it projects an image of *C* and *D* for 45° linearly polarized light, and left circularly polarized light respectively.

To design the device, we first developed a new algorithm to compute the required Jones matrix profile. It is a gradient-descent-based optimization method which is generalized from the well-known Gerchberg-Saxton phase retrieval algorithm [16] (Appendix, Sec. 2). Note that this algorithm considers the target intensity profiles for different incident polarization states, instead of the far field Jones matrix distribution. The latter is discussed in another work in Ref. [27]. The optimized Jones matrix profile is shown in Fig. 4(c). One can see that the points are scattered around in the unity ball. This tells us two things: first, this is a nonseparable transformation, since the points do not belong to an ellipse [Fig. 2(b)]; second, a double-layer metasurface is required for the implementation, as the points do not belong to an ellipsoid either [Fig. 2(e)]. More details on how to compute and utilize the retarder parameters can be found in the Appendix, Secs. 1.3.1 and 3.2.

To implement the device, we simulated a library of double-layer nanostructures. A schematic of the building blocks is shown in Fig. 4(b). It consists of two layers of TiO_2 rectangular nanopillars fabricated on top of one another. In each layer, the nanopillar length (L_t , L_b), width (W_t , W_b), and angular orientation (θ_t , θ_b) can vary arbitrarily and independently. One can see that the points densely occupy the entire retarder space [Fig. 4(d)], proving their capability of realizing any polarization wave front transformation.

Lastly, we need to fit the target profile using the library. At each location on the metasurface, we search for a structure in the library that best matches the target Jones matrix. The simulated output far field intensity profiles are shown in Figs. 4(e)–4(h). Four different letters—*A*, *B*, *C*, *D*—are projected for horizontal, vertical, 45 degree, and left circular incident polarization respectively.

We denote the output fields for horizontal and vertical incident polarization as \vec{E}_H and \vec{E}_V . Their polarization distribution is illustrated in Figs. 4(i)–4(j). Clearly, the local orthogonality is not satisfied. For 45 degree incident polarization, the output field is $\vec{E}_{45^\circ} = (1/\sqrt{2})(\vec{E}_H + \vec{E}_V)$. Its intensity is given by

$$|\vec{E}_{45^\circ}|^2 = \frac{1}{2}(|\vec{E}_H|^2 + |\vec{E}_V|^2) + \text{Re}[\vec{E}_H^* \cdot \vec{E}_V]. \quad (4)$$

Similarly, for left circular polarization incidence,

$$|\vec{E}_{\text{LCP}}|^2 = \frac{1}{2}(|\vec{E}_H|^2 + |\vec{E}_V|^2) - \text{Im}[\vec{E}_H^* \cdot \vec{E}_V]. \quad (5)$$

The interference term—the real and imaginary part of $\vec{E}_H^* \cdot \vec{E}_V$ —is shown in Figs. 4(k)–4(l). One can see that destructive interference (blue) suppresses the unwanted pattern, and that constructive interference (red) occurs in the desired area.

In the Appendix, we show that more than four holographic images can be encoded in a single device, at the expense of more crosstalk (Design 1–3 in Fig. S4, Supplemental Material [19]). Note that for illustration purposes, we do not rely on any postselection of polarization, that is, there is no polarizer after the metasurface. With postselection polarizers, the crosstalk can be further reduced (Design 4 in Fig. S4, Supplemental Material [19]), but it comes at the expense that additional information about the postselection states has to be provided in order to successfully retrieve the holographic images.

Discussion.—In principle, the polarization function of a double-layer metasurface can also be realized by cascading multiple single-layer metasurfaces in sequence. In practice, however, the optical alignment requirement can be very challenging to meet, especially for holographic applications where the required Jones matrix profiles may vary rapidly at the subwavelength scale.

Besides metasurfaces, there are many other types of polarization elements, such as liquid crystal (LC) devices [1]. LC is tunable and low cost, but offers fewer design degrees of freedom for polarization control. Typically only one parameter—either phase retardation or the optical axis orientation—can be controlled spatially. Therefore, four cascaded LC components are required to realize a general polarization transformation [28].

For simplicity, in this manuscript we choose to work in the weak coupling regime—the interaction between nanostructures in different layers is negligible. It is, however, also possible to enhance and utilize interlayer coupling to realize novel optical responses such as angle-dependent polarization control [9] and exceptional points [29].

This material is based on work supported by the Air Force Office of Scientific Research under Grant No. FA9550-19-1-0135. J.S.P. is on leave from Korea Institute of Science and Technology. Z.S. gratefully acknowledges Dr. Zhehao Dai for insightful comments and discussions.

-
- [1] D.-K. Yang and S.-T. Wu, *Fundamentals of Liquid Crystal Devices* (John Wiley & Sons, New York, 2014).
 [2] J. Kim, Y. Li, M. N. Miskiewicz, C. Oh, M. W. Kudenov, and M. J. Escuti, Fabrication of ideal geometric-phase holograms with arbitrary wavefronts, *Optica* **2**, 958 (2015).
 [3] L. Nikolova and P. Ramanujam, *Polarization Holography* (Cambridge University Press, Cambridge, England, 2009).

- [4] A. W. Lohmann, Reconstruction of vectorial wavefronts, *Appl. Opt.* **4**, 1667 (1965).
 [5] E. Maguid, I. Yulevich, D. Veksler, V. Kleiner, M. L. Brongersma, and E. Hasman, Photonic spin-controlled multifunctional shared-aperture antenna array, *Science* **352**, 1202 (2016).
 [6] A. Arbabi, Y. Horie, M. Bagheri, and A. Faraon, Dielectric metasurfaces for complete control of phase and polarization with subwavelength spatial resolution and high transmission, *Nat. Nanotechnol.* **10**, 937 (2015).
 [7] J. P. Balthasar Mueller, N. A. Rubin, R. C. Devlin, B. Groever, and F. Capasso, Metasurface Polarization Optics: Independent Phase Control of Arbitrary Orthogonal States of Polarization, *Phys. Rev. Lett.* **118**, 113901 (2017).
 [8] J. N. Damask, *Polarization Optics in Telecommunications* (Springer Science & Business Media, Springer New York, 2004), Vol. 101.
 [9] Z. Shi, A. Y. Zhu, Z. Li, Y.-W. Huang, W. T. Chen, C.-W. Qiu, and F. Capasso, Continuous angle-tunable birefringence with freeform metasurfaces for arbitrary polarization conversion, *Sci. Adv.* **6**, eaba3367 (2020).
 [10] R. Chipman, Chapter 22-Polarimetry, *Handbook of Optics*, edited by M. Bass (McGraw-Hill New York, 1995), Vol. II.
 [11] C. Menzel, C. Rockstuhl, and F. Lederer, Advanced jones calculus for the classification of periodic metamaterials, *Phys. Rev. A* **82**, 053811 (2010).
 [12] R. J. Potton, Reciprocity in optics, *Rep. Prog. Phys.* **67**, 717 (2004).
 [13] R. A. Chipman, W.-S. T. Lam, and G. Young, *Polarized Light and Optical Systems* (CRC Press, Boca Raton, 2019).
 [14] V. Liu and S. Fan, S⁴: A free electromagnetic solver for layered periodic structures, *Comput. Phys. Commun.* **183**, 2233 (2012).
 [15] I. Moreno, M. J. Yzuel, J. Campos, and A. Vargas, Jones matrix treatment for polarization fourier optics, *J. Mod. Opt.* **51**, 2031 (2004).
 [16] J. R. Fienup, Phase retrieval algorithms: A comparison, *Appl. Opt.* **21**, 2758 (1982).
 [17] N. A. Rubin, G. D’Aversa, P. Chevalier, Z. Shi, W. T. Chen, and F. Capasso, Matrix fourier optics enables a compact full-stokes polarization camera, *Science* **365**, eaax1839 (2019).
 [18] R. C. Jones, A new calculus for the treatment of optical systems. i. description and discussion of the calculus, *J. Opt. Soc. Am.* **31**, 488 (1941).
 [19] See Supplemental Material at <http://link.aps.org/supplemental/10.1103/PhysRevLett.129.167403> for more detailed definitions, derivations and proofs regarding polarization wave front transformations.
 [20] N. Yu, P. Genevet, M. A. Kats, F. Aieta, J. P. Tetienne, F. Capasso, and Z. Gaburro, Light propagation with phase discontinuities: Generalized laws of reflection and refraction, *Science* **334**, 333 (2011).
 [21] A. V. Kildishev, A. Boltasseva, and V. M. Shalaev, Planar photonics with metasurfaces, *Science* **339**, 1232009 (2013).
 [22] Q. Fan, M. Liu, C. Zhang, W. Zhu, Y. Wang, P. Lin, F. Yan, L. Chen, H. J. Lezec, Y. Lu, A. Agrawal, and T. Xu, Independent Amplitude Control of Arbitrary Orthogonal States of Polarization via Dielectric Metasurfaces, *Phys. Rev. Lett.* **125**, 267402 (2020).

- [23] Y. Yuan, K. Zhang, B. Ratni, Q. Song, X. Ding, Q. Wu, S. N. Burokur, and P. Genevet, Independent phase modulation for quadruplex polarization channels enabled by chirality-assisted geometric-phase metasurfaces, *Nat. Commun.* **11**, 1 (2020).
- [24] H. Kwon, E. Arbabi, S. M. Kamali, M. Faraji-Dana, and A. Faraon, Single-shot quantitative phase gradient microscopy using a system of multifunctional metasurfaces, *Nat. Photonics* **14**, 109 (2020).
- [25] H. Ren, G. Briere, X. Fang, P. Ni, R. Sawant, S. Héron, S. Chenot, S. Vézian, B. Damilano, V. Brändli *et al.*, Metasurface orbital angular momentum holography, *Nat. Commun.* **10**, 1 (2019).
- [26] Y. Zhou, I. I. Kravchenko, H. Wang, H. Zheng, G. Gu, and J. Valentine, Multifunctional metaoptics based on bilayer metasurfaces, *Light. Light.* **8**, 1 (2019).
- [27] N. A. Rubin, A. Zaidi, A. Dorrah, Z. Shi, and F. Capasso, Jones matrix holography with metasurfaces, *Sci. Adv.* **7**, abg7488 (2021).
- [28] A. Sit, L. Giner, E. Karimi, and J. S. Lundeen, General lossless spatial polarization transformations, *J. Opt.* **19**, 094003 (2017).
- [29] A. Cerjan and S. Fan, Achieving Arbitrary Control Over Pairs of Polarization States Using Complex Birefringent Metamaterials, *Phys. Rev. Lett.* **118**, 253902 (2017).